OPEN

Engineering nanocolumnar defect configurations for optimized vortex pinning in high temperature superconducting nanocomposite wires

Sung Hun Wee[1], Yuri L. Zuev[2], Claudia Cantoni[1] & Amit Goyal[1]

[1]Materials Science and Technology Division, Oak Ridge National Laboratory, Oak Ridge, TN 37831-6116, USA, [2]Department of Physics, University of Tennessee, Knoxville, TN 37996, USA.

We report microstructural design via control of BaZrO$_3$ (BZO) defect density in high temperature superconducting (HTS) wires based on epitaxial YBa$_2$Cu$_3$O$_{7-\delta}$ (YBCO) films to achieve the highest critical current density, J_c, at different fields, H. We find the occurrence of $J_c(H)$ cross-over between the films with 1–4 vol% BZO, indicating that optimal BZO doping is strongly field-dependent. The matching fields, B_ϕ, estimated by the number density of BZO nanocolumns are matched to the field ranges for which 1–4 vol% BZO-doped films exhibit the highest $J_c(H)$. With incorporation of BZO defects with the controlled density, we fabricate 4-μm-thick single layer, YBCO + BZO nanocomposite film having the critical current (I_c) of ~1000 A cm^{-1} at 77 K, self-field and the record minimum I_c, I_c(min), of 455 A cm^{-1} at 65 K and 3 T for all field angles. This I_c(min) is the largest value ever reported from HTS films fabricated on metallic templates.

Synthesis of epitaxial nanocomposite films containing self-assembled, ordered arrays of nanodots/nanorods/nanopillars of one type of complex material embedded in another complex functional material has stimulated research in a wide range of application areas such as multiferroics, magnetoelectrics, thermoelectrics, ultra-high density storage, and high temperature superconductors[1–5]. In these application areas, the nanocomposite films can offer new or significantly enhanced functionalities which are not attainable from individual materials or phases comprising the composite. One of the fascinating examples is high temperature superconducting (HTS) nanocomposites based on YBa$_2$Cu$_3$O$_{7-\delta}$ (YBCO) containing a few volume% (vol%) insulating columnar defects comprised of simple or double perovskite-structured materials with simple (or distorted) cubic structure that include BaZrO$_3$ (BZO), BaSnO$_3$, Ba$_2$RETaO$_6$, and Ba$_2$RENbO$_6$[5–12]. Driscoll *et al.*[13] were the first to demonstrate that incorporation of randomly oriented, disk shaped BZO nanoparticles with a modal size of ~10 nm was beneficial to pinning[13]. It was subsequently demonstrated that spontaneous self-assembly of well-ordered, vertically aligned, nanocolumns parallel to the YBCO *c*-axis was possible by incorporation of the materials listed above[5–12] and that such self-assembly occurs via spontaneous phase separation and a strain-driven ordering process driven by minimization of strain fields arising from the lattice mismatch (5 ~ 12%) between the embedded nanophase and the YBCO matrix[14]. Since these columnar defects typically form ordered arrays of columns with diameters (5 ~ 10 nm) comparable to the diameter of a magnetic vortex core $\approx 2 \times \xi(T)$, ($\xi(T) =$ superconducting coherent length for YBCO, $\xi^2(T) \approx \xi^2(0) \dfrac{1}{1 - T/T_C}$, $\xi(0) = 1.5 \sim 2$ nm), they effectively pin or immobilize magnetic flux lines (or vortices), resulting in a dramatic improvement of the critical current density, J_c, in the presence of applied magnetic fields, particularly when the field is parallel to the orientation of the aligned defects, $H \| c$-axis[5–12].

HTS wires based on YBCO nanocomposite films are an essential component to realize a wide range of environmentally friendly, highly efficient electric power devices with small weight and footprint[15]. Since the field and temperature regimes in which these devices are operated are different[15], vortex pinning via columnar defects needs to be tailored to achieve the highest J_c at the desired fields and temperatures required by the specific applications. An ideal strategy to achieve such a goal is to incorporate as many columnar defects as the number of vortices generated at the operating magnetic field. Fewer defects would leave unpinned vortices, and extra defects would compromise the volume of superconducting phase, both limiting J_c[16]. Since vortex spacing depends on the

magnetic field strength, nanocolumn spacing to accommodate all vortices is expected to be field-dependent. For this reason, the effect of BZO nanocolumn density on the J_c as a function of magnetic field strength, orientation, and operating temperature needs to be comprehensively understood. Ultimately, we should be able to tailor the BZO defect density to achieve an optimal superconducting performance at a given application specific, operating temperature and applied magnetic field. Although previous work has reported the importance of controlling the columnar defect density to enhance and tailor the in-field J_c properties[17–20], there is no report of systematic variation of the optimal columnar defect density as a function of magnetic field strength, orientation, and operating temperature.

In the present work, we show that the density of BZO columnar defects necessary to achieve optimal J_c performance systematically increases with increasing magnetic field and is also influenced by field orientation and temperature. In addition, we demonstrate that a single layer 4-μm-thick YBCO films with the controlled density of BZO nanocolumns exhibits excellent critical current (I_c) performance given by a I_c of ∼1000 A cm^{-1} at 77 K, self-field and a minimum I_c, I_c(min), of 455 A cm^{-1} at 65 K and 3 T for all magnetic field orientations. Such high I_c(min) at 65 K and 3 T is the record value ever reported from HTS films fabricated on metallic templates.

Results

Engineering BZO nanocolumnar defect density for J_c optimization at different fields. Figure 1 summarizes X-ray diffraction results for YBCO films with different BZO contents up to 10 vol%. All samples with same thickness of ∼0.8 μm were deposited on LMO/IBAD-MgO/Hastelloy templates via pulsed laser deposition (PLD). The detailed procedures of the samples preparation are summarized in the Experimental section. The θ–2θ scans (Fig. 1a) show that all films have sharp out-of-plane c-axis orientation with strong (00l)

peak intensities of YBCO phase. For BZO-doped samples, additional peaks at $2\theta = 21.6°$ (which is evident only for the 10 vol% BZO-doped sample due to the large concentration of BZO phase) and 43.3° correspond to (001) and (002) BZO peaks indicating the formation of epitaxial BZO nanophase within the YBCO matrix. The narrow scans (Fig. 1b) for BZO (002) peak measured at the maximum X-ray power show evidently stronger peak intensities with increasing BZO addition, despite the slight peak overlap with the MgO (200) peak, which stems from the epitaxial MgO layer comprising the template. Detailed XRD analysis based on peak broadening estimates that the size of BZO nanophase is ∼6–7 nm and remains nearly unchanged up to 10 vol% BZO. Figure 1c shows the summary of full-width-half-maximum of omega and phi scans (Δω and Δφ) for YBCO and BZO phases taken from the samples. Essentially, no meaningful variation of Δω and Δφ in both YBCO phase and BZO nanophase is measured from all BZO-doped films. The Δω and Δφ values of YBCO phase are in the ranges of 1.3° ∼ 2° and 3.2° ∼ 3.6°, respectively, while those of the BZO nanophase range from 2.1° to 2.8° and from 5.8° to 6.2°, respectively. Relatively larger Δω and Δφ for the BZO nanophase should be attributed to the deviation of their alignments with respect to the in-plane and out-of-plane of YBCO film as well as the substrate[10]. Although the ω and φ scan results imply that all samples with BZO contents up to 10 vol% have good epitaxial YBCO phase with similar in-plane and out-of-plane textures, YBCO (113) pole figure measurements (Fig. 1d) reveal that texture degradation occurs when BZO content increases to 10 vol%. Unlike the 1–4 vol% BZO-doped samples having only strong, sharp four-fold symmetric peaks, the 10 vol% BZO-doped film exhibits an additional texture component indicated by a circular pattern along with the four-fold symmetric peaks, mostly caused by formation of misoriented and 45° rotated grains. A quantitative fraction (%cube-texture) of "cube-textured"
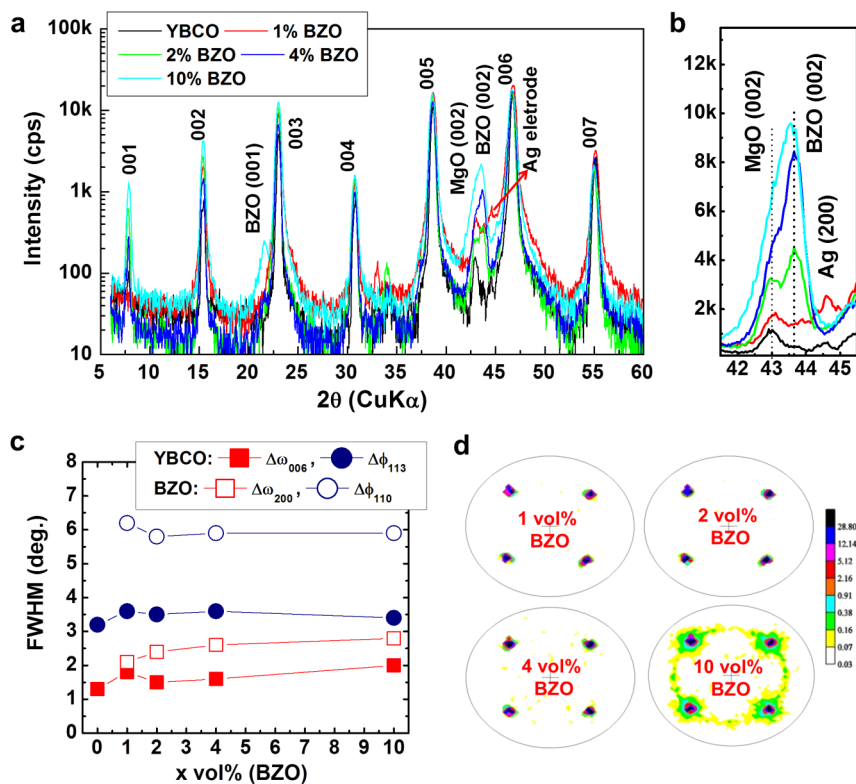

Figure 1 | X-ray diffraction results for YBCO films with different BZO additions. (a) θ–2θ scans for the samples at X-ray power (−50 kV, 5 mA) where the intensity of (006) YBCO peak does not exceed the maximum intensity limit of the detector. (b) θ–2θ scans from 2θ = 41.5° to 45.5° at maximum X-ray power (-50 kV, 30 mA). (c) Δω and Δφ values for YBCO phase and BZO nanophase for the films with and without BZO additions. (d) YBCO (113) pole figures for 1–10 vol% BZO-doped samples.

volume out of the total volume of the layer was determined by the numerical method described elsewhere[21]. The 10 vol% BZO doped sample only has 90% cube-texture which is smaller than the values of 95 ~ 96% typically measured from un-doped and 1–4 vol% BZO-doped films.

Transmission electron microscopy (TEM) examination confirms the formation of self-aligned BZO nanocolumns in YBCO + BZO nanocomposite films. As shown in Figs. 2a and 2c, cross-section TEM images for the 1 and 4 vol% BZO-doped films show BZO nanocolumns, well-ordered and in general aligned to the crystallographic c-axis of YBCO with some splayed feature with respect to the c-axis similar to previous reports[7,10]. Figure 2b shows a plan-view TEM image for the 2 vol% BZO-doped film containing moiré fringes caused by BZO nanoparticles which are sections of BZO nanocolumns. The TEM images confirm the increase in the columnar defect density with BZO content while their average diameters remain unchanged around 5–6 nm, consistent with the estimated values by XRD. Figure 2d shows a summary of average BZO nanocolumn spacing, d, for 1–4 vol% BZO doped samples, based on the examination of several TEM images collected from the samples containing different BZO contents. With the nanocolumn spacing, we calculated the matching field, $B_\phi = 2\Phi_0/\sqrt{3}a^2$ as ~0.8 T for 1 vol% BZO, ~6 T for 2 vol% BZO, and ~15 T for 4% BZO-doped samples, where $\Phi_0 = 2.07 \times 10^{-11}$ T cm² is the flux quantum and a is the vortex spacing that matches d at B_ϕ.

When BZO doping is further increased to 10 vol%, we observed a morphological change in the array of BZO defects as shown in Fig. 3. Essentially, some BZO defects start to be aligned horizontally (along ab-planes) along with BZO nanocolumns aligned vertically (along c-axis) denoted by blue and red arrows (Fig. 3a). Since the imaging conditions that bring out BZO defects aligned vertically and horizontally are slightly different, the defects aligned to the ab-planes are more clearly observed in a different image of the same specimen taken from different imaging conditions (Fig. 3b). Vertically aligned BZO nanocolumns are very dense, and the average BZO column spacing can be estimated to be less than 10 nm, much narrower than that for the 4 vol% BZO-doped sample. The appearance of semi-continuous, planar BZO defect arrays is anticipated when the BZO doping concentration is high enough to minimize the distance between adjacent BZO nanodots nucleating within the same ab-plane, as shown in our previous work[14]. Further increase in BZO content is expected to produce continuous planar BZO layers in the YBCO matrix. Indeed, YBCO/BZO multilayer structure containing planar BZO defects arrays was reported from YBCO + BZO nanocomposite films with high BZO concentration such as 50 mol% YBCO and 50 mol% BZO[22].

Table 1 summarizes superconducting transition temperature, T_c, and self-field J_c at 77 K and 65 K for the set of un-doped and BZO-doped YBCO films with different BZO contents. Note that as denoted in Table 1, 1 vol% BZO is equivalent to 1 wt% and 2.4 mol% BZO. Several 0.5 and 1 vol% BZO-doped films are reproducibly measured to have T_c of 87.5 ~ 87.7 K, essentially unchanged from those ($T_c = 87.5$ ~ 88.0 K) obtained from pure YBCO films grown on IBAD-MgO templates in identical PLD conditions. When BZO doping is over 1 vol%, T_c starts to drop monotonically with a drop rate of ~0.46 K/vol% (0.2 K/mol%). In a previous work[23], we suggested that the origin of T_c reduction with increasing BZO doping should be attributed to local strain field caused by the lattice mismatch (~8%) between YBCO and BZO phases and the consequent local oxygen deficiency that possibly occurs around BZO nanocolumns. Microstrain measurement of BZO-doped samples based on Williamson-Hall plots[24,25] shows that the strain field monotonically
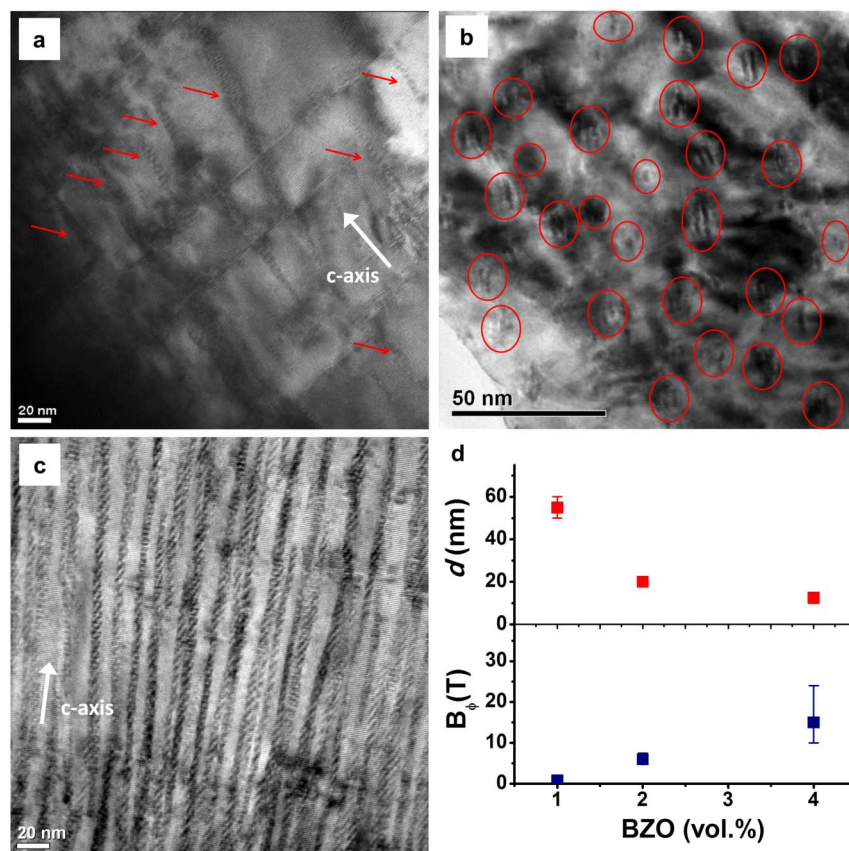

Figure 2 | Typical cross-sectional and plan-view TEM micrographs for YBCO + BZO nanocomposite films. (a) and (c) Cross-sectional TEM images of 1 and 4 vol% BZO-doped films respectively. (b) Plan-view TEM image for 2 vol% BZO-doped film. (d) Average BZO nanocolumn spacing, d, and corresponding matching field, B_ϕ, as a function of BZO doping concentration.
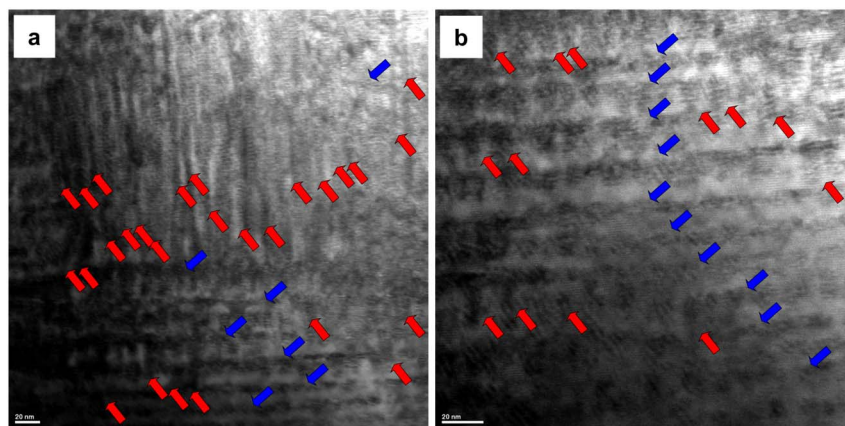
Figure 3 | Cross-sectional TEM micrographs for 10 vol% BZO-doped film. (a) An image shows semi-continuous BZO nanodots arrays aligned to the *ab*-planes as well as dense BZO nanocolumns aligned to the *c*-axis of the film. (b) An image taken from the same TEM specimen at a different image condition highlights more clearly planar BZO defects aligned to the *ab*-planes. Note that some of BZO defects aligned vertically and horizontally are denoted as red and blue arrows.

increases as BZO content increases[23]. High resolution, scanning TEM analysis confirms that a local area surrounding a BZO nanocolumn having approximately an outer diameter of $\sim$15–20 nm, is highly strained and also oxygen deficient[23]. When average BZO columns spacing is near or above this diameter by increasing BZO doping, an overlap of strained REBCO regions surrounding BZO nanocolumns is expected to occur, and T_c starts to decrease. As aforementioned, the BZO doping level that results in the average BZO column spacing near or above $\sim$15–20 nm is around 2–4 vol%, which is the concentration at which T_c apparently starts to decrease. For the self-field J_c at 77 K and 65 K, the J_c values are noticeably improved with BZO doping up to 1 vol%. The highest J_c of 4.1 MA cm^{-2} at 77 K and 12.2 MA cm^{-2} at 65 K are achieved from the 1 vol% BZO-doped sample. After an initial enhancement, the J_c gradually degrades up to 0.34 MA cm^{-2} at 77 K with further increasing BZO up to 10 vol%. Such J_c variation suggests that even at self-field, additional BZO defects enhance the pinning and J_c performance of the films, and 1 vol% BZO is an optimum doping level resulting in the highest J_c at 77 K and 65 K.

In the presence of applied magnetic fields, the strong dependence of the optimum BZO doping level on the applied magnetic field strength is observed. Figure 4 shows J_c and pining force (F_p) as a function of applied magnetic field, $J_c(H)$ and $F_p(H)$, for YBCO films with different BZO contents, for the field parallel to YBCO *c*-axis, ($H\|c$) at 77 K and 65 K. The inset of Fig. 4a also displays the normalized $J_c(H)$ data at 77 K to determine α values in the power-law dependence of J_c on H, $J_c \sim H^{-\alpha}$ valid in the range of $\sim$0.2–1.5 T, which are also summarized in Table 1. Compared to the un-doped sample, the 1–4 vol% BZO-doped samples show a significantly improved $J_c(H)$, much higher $F_p(H)$, and smaller α values, indicating

the efficacy of BZO columnar defects as strong *c*-axis pinning centers. The highest F_p(max) values of 9.5 GN m^{-3} at 77 K, 2 T and 74 GN m^{-3} at 65 K, 5 T as well as the smallest α value of $\sim$0.33 are obtained from the 2 vol% BZO-doped sample. Unlike these samples, 10 vol% BZO-doped sample shows much poorer $J_c(H)$ and $F_p(H)$ at both temperatures, primarily due to the detrimental problems caused by excess BZO doping as will be discussed later. Another essential feature observed in the figures is the occurrence of $J_c(H)$ (or $F_p(H)$) cross-over between the films with 1–4 vol% BZO, indicating that the optimal BZO doping is strongly field-dependent. The $J_c(H)$ data at 77 K show that the 1 vol% BZO-doped film has the highest $J_c(H)$ in the self-field and up to the first cross-over field of $\sim$1.6 T. When the field is higher than $\sim$1.6 T, the 2 and 4 vol% BZO doping levels lead to the highest $J_c(H)$ up to and over the second cross-over field of $\sim$7.3 T, respectively. $J_c(H)$ data at 65 K also show the same trend, but the cross-over fields are moved to higher fields as indicated in the figure.

Figures 5a–5c show angular dependent J_c, $J_c(\theta)$, for the samples at different temperatures and field regimes. The measurement was made in the maximum Lorentz force configuration in which the applied field direction is always perpendicular to the direction of current flow. 1–4 vol% BZO-doped films show higher $J_c(\theta)$ than the un-doped sample for the entire angular range. In addition to higher $J_c(\theta)$ at and near $H\|c$ stemming directly from strong *c*-axis correlated pinning via BZO nanocolumnar defects, the overall improvement in $J_c(\theta)$ for angles away from $H\|c$ can be attributed to the enhanced pinning via strong BZO defect-vortex interaction that still exist, although the pinning strength gradually decreases due to the reduced area of vortex confined by BZO columns with angles away from $H\|c$[16]. This is the primary reason why the enhancement in $J_c(\theta)$ near $H\|ab$ for 2 and 4 vol% BZO-doped samples is limited and eventually negligible at 65 K, 3 and 5 T. Despite this fact, the 1 vol% BZO-doped sample maintains higher $J_c(\theta)$ near $H\|ab$ than the 2 and 4 vol% BZO-doped samples, which lead to the highest J_c(min) for all field orientations, as shown in Fig. 5d. Note that the J_c(min) is considered a critical performance parameter particularly for devices with wound wire architectures such as motors, generators, and high field magnets, so that HTS wires having higher J_c(min) are more desirable for these device applications.

Growth of thick YBCO films with engineered nanocolumns. Considering $J_c(H,\theta,T)$ data for $\sim$0.8 μm thick YBCO nanocomposite films with different BZO contents reported in Figs. 4 and 5, we grew $\sim$4-μm-thick YBCO films containing 1 vol% BZO in order to achieve superior I_c performance at self-field and in

Table 1 | Transport T_c, self-field J_c at 77 K and 65 K, and α values for 0.8 μm thick YBCO + BZO nanocomposite films grown on IBAD-MgO templates via PLD

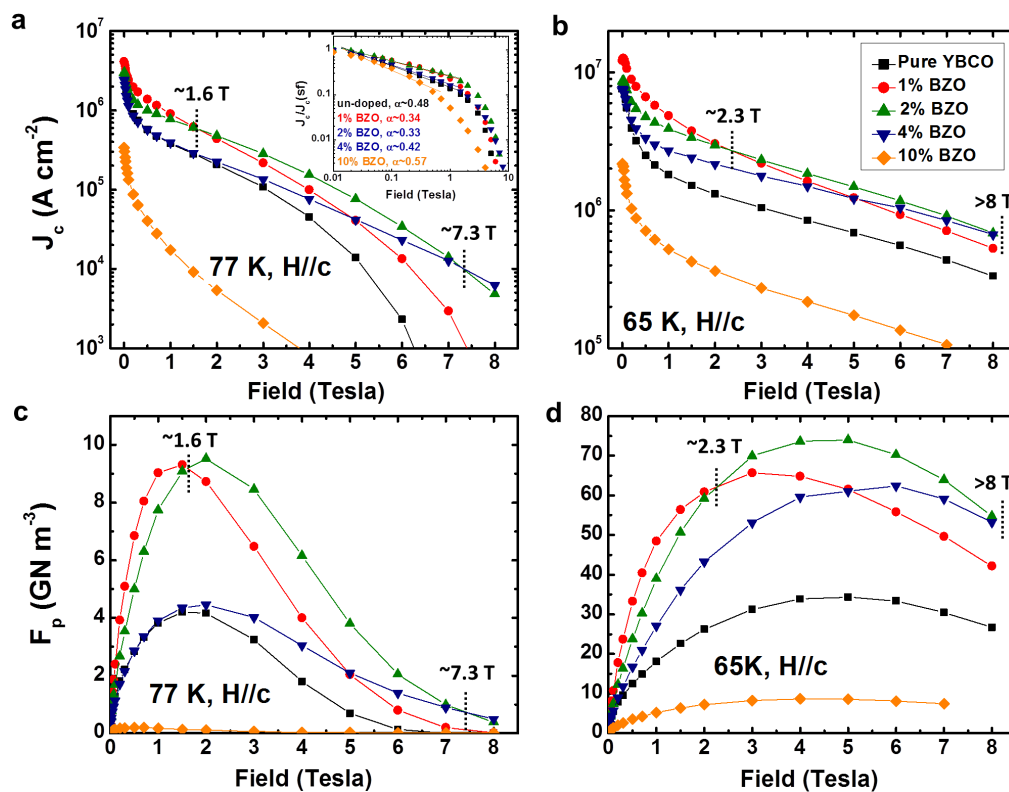| YBCO + x vol.% BZO	mol%	T_c (K)	J_c (77 K,sf) (MA cm^{-2})	J_c (65 K,sf) (MA cm^{-2})	α, $J_c \sim H^{-\alpha}$ (77 K, $H\|c$)
Pure YBCO	0	87.7	2.8	7.6	0.48
0.5 vol% BZO	1.2	87.5	3.2	8.1	0.41
1 vol% BZO	2.4	87.7	4.1	12.2	0.34
2 vol% BZO	4.8	86.6	3.0	8.6	0.33
4 vol% BZO	9.6	84.9	2.4	7.4	0.42
10 vol% BZO	24	83.6	0.34	2.2	0.57

Figure 4 | Field dependent J_c and F_p for $H//c$ with the magnetic field up to 8 T for pure YBCO and YBCO + 1–10 vol% BZO films. (a) $J_c(H)$ at 77 K, (b) $J_c(H)$ at 65 K, (c) $F_p(H)$ at 77 K, and (d) $F_p(H)$ at 65 K. The inset of Fig. 4(a) shows normalized J_c, $J_c(H)/J_c(sf)$, for the samples. All samples have an identical film thickness of ~0.8 μm.
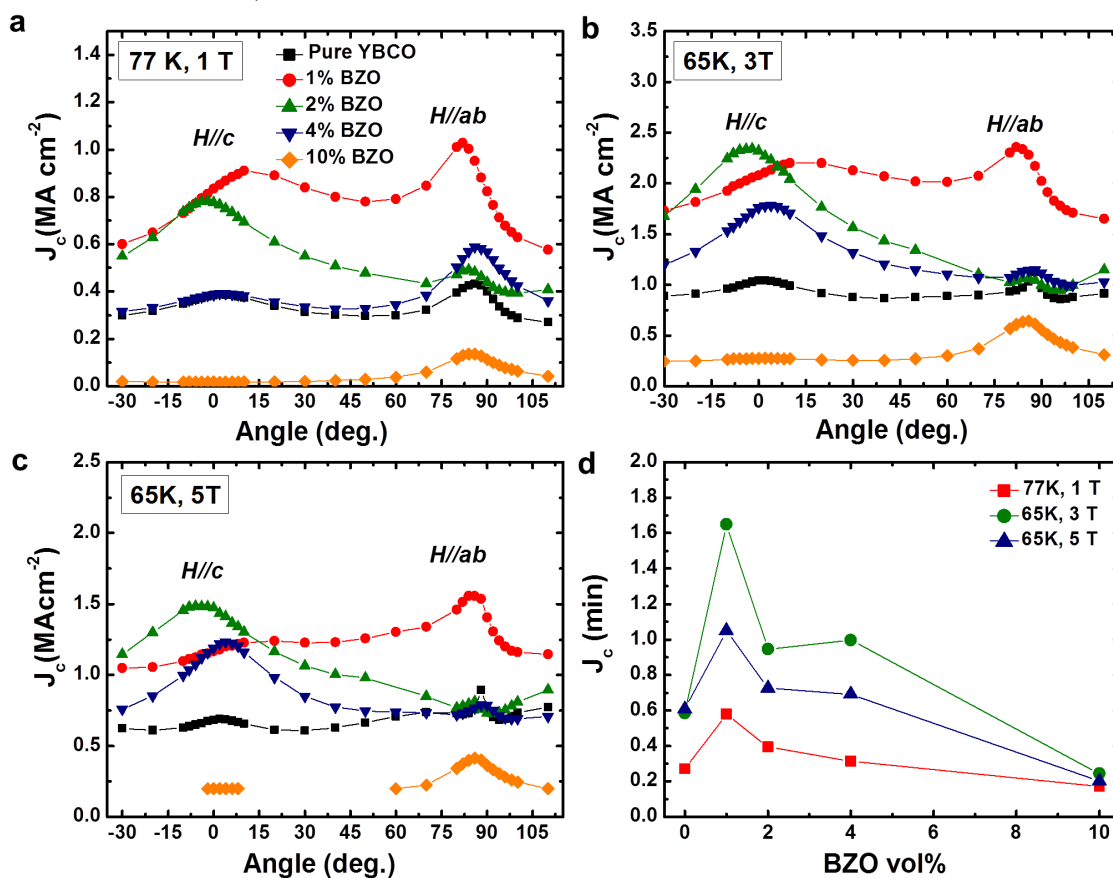

**Figure 5 | The angular dependent J_c at (a) 77 K, 1 T, (b) 65 K, 3 T, and (c) 65 K, 5 T for pure YBCO and YBCO + 1–10 vol% BZO films, in magnetic field applied −30° to 110° with respect to the c-axis of the film. (d) $J_c(min)$ for all field orientation for YBCO nanocomposite films with different BZO additions.

moderate magnetic field range of 0.5–3 T at 77 K and 65 K. To quantitatively evaluate the performance improvement by incorporating BZO defects, 4-μm-thick, un-doped films were also prepared in identical growth conditions. Phase and microstructural properties for both 4-μm-thick HTS films with and without 1 vol% BZO are summarized in Fig. 6. The most striking difference in structural properties between the un-doped and BZO-doped samples is the amount of a-axis oriented grains which are one of the major detrimental factors precluding a proportional increase of I_c with thickness[26]. Quantitative volumetric amount of a-axis grains in the films is determined by XRD, comparing the intensity of (001) normal with (100) normal peaks obtained in YBCO (102) χ-scans, $I_{(100)}/[I_{(001)} + I_{(100)}] \times 100$, as shown in Fig. 6b. The BZO-doped thick film is measured to have only ~3 vol% of a-axis oriented grains which is remarkably reduced from ~30 vol% of a-axis oriented grains measured from the un-doped thick sample. Plan-view scanning electron microscopy images (Figs. 6c and 6d) show that the BZO-doped thick film has denser and smoother surface morphology with significantly reduced a-axis oriented surface particles/grains compared to the un-doped thick film.

Figure 7 shows transport I_c versus magnetic field at 77 K and 65 K for 4-μm-thick films with and without 1 vol% BZO. The I_c data at 75.5 K for the film containing 1 vol% BZO were also measured and shown in the inset of Fig. 7b for comparison with the previously reported high I_c data at 75.5 K[27,28]. The BZO-doped thick film has the self-field I_c values of 995 A cm^{-1} at 77 K and 1188 A cm^{-1} at 75.5 K, which correspond to the J_c of 2.5 and 3 MA cm^{-2}, respectively. The self-field I_c at 77 K for the BZO-doped sample is more than twice as large as the I_c of 465 A cm^{-1} of the un-doped thick film. In fact, multiple samples containing 1 vol% BZO showed the self-field I_c of 750 ~ 1000 A cm^{-1} at 77 K, while un-doped samples have the I_c of 450 ~ 530 A cm^{-1}. Due to a limit in the maximum current (~25 A) that can be applied to the patterned sample (215 μm in width), the self-field I_c at 65 K cannot be directly measured. However, the I_c over 1000 A cm^{-1} at 65 K are retained at fields up to 1 T for $H\|c$ and 1.5 T for $H\|ab$. In the presence of applied magnetic fields, superior $I_c(H)$ with excellent I_c retention properties can be seen in the BZO-doped thick sample, compared to the un-doped thick film. At 77 K, 1 T, the I_c of ~ 340 A cm^{-1} for $H\|c$ is only reduced by a factor of ~2.9 from the I_c at self-field, indicating a massive enhancement in pinning via BZO columnar defects. At 65 K, the I_c for $H\|c$ and $H\|ab$ are well over 150 A cm^{-1} at fields up to 8 T. All these I_c values are 2- or 3-fold larger than those for the un-doped thick sample.

Angular dependent I_c at 77 K, 1 T and 65 K, 3 T are shown in Fig. 8. Compared to the un-doped thick film, the BZO-doped thick film shows the remarkably improved I_c for all field angles. The BZO-doped thick film has the I_c(min) of 196 A cm^{-1} at 77 K, 1 T and 455 A cm^{-1} at 65 K, 3 T which are about three times larger than those for the un-doped thick film. At 75.5 K, 1 T, the BZO-doped film is also measured to have the I_c(min) of 251 A cm^{-1} (the data not shown here) which is nearly 30% increase in the value at 77 K, 1 T.

Discussion

Since B_ϕ is the field at which the density of vortices matches that of the BZO nanocolumns, Figure 2d provides key information on how
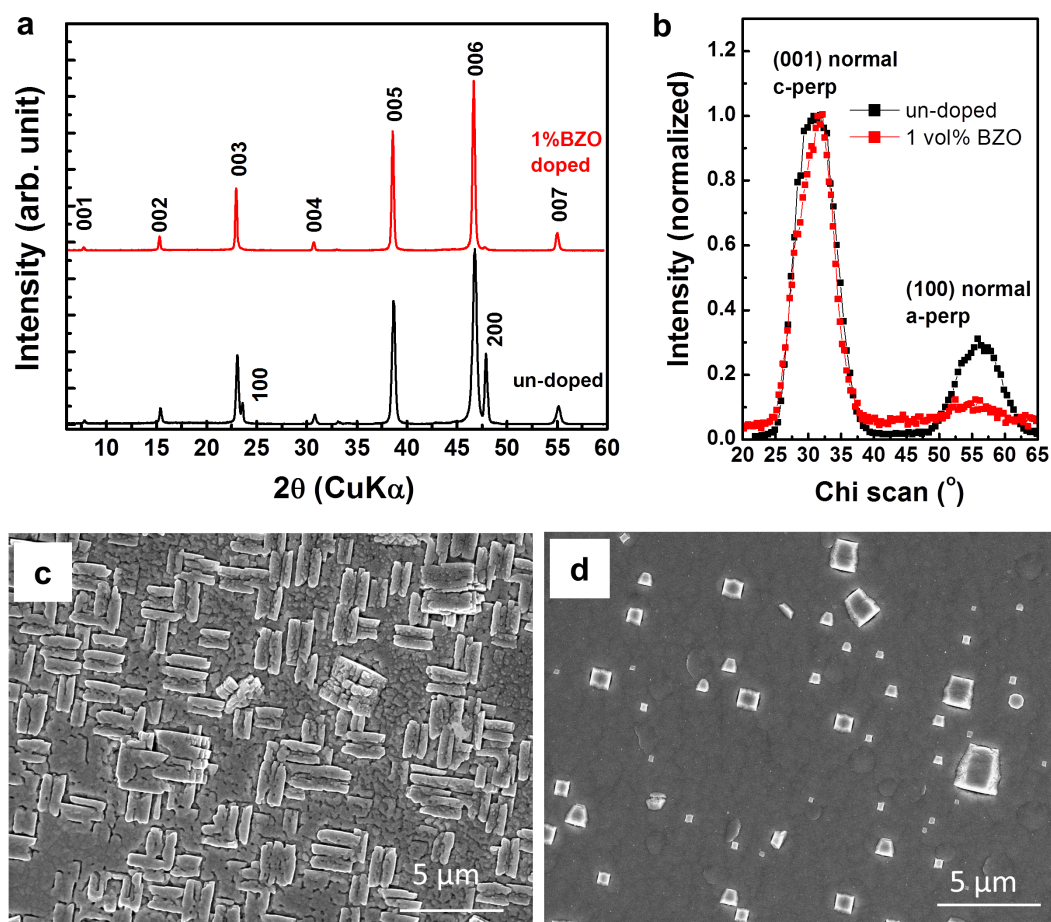

Figure 6 | (a) θ–2θ scans and (b) (102) χ-scans for un-doped and 1 vol% BZO-doped, 4 μm thick YBCO films. Plan-view SEM images for (c) un-doped and (d) 1 vol% BZO-doped, 4 μm thick YBCO films on IBAD-MgO template with LaMnO$_3$ cap layer. The results indicate that the a-axis growth in thick films is significantly suppressed by BZO addition.
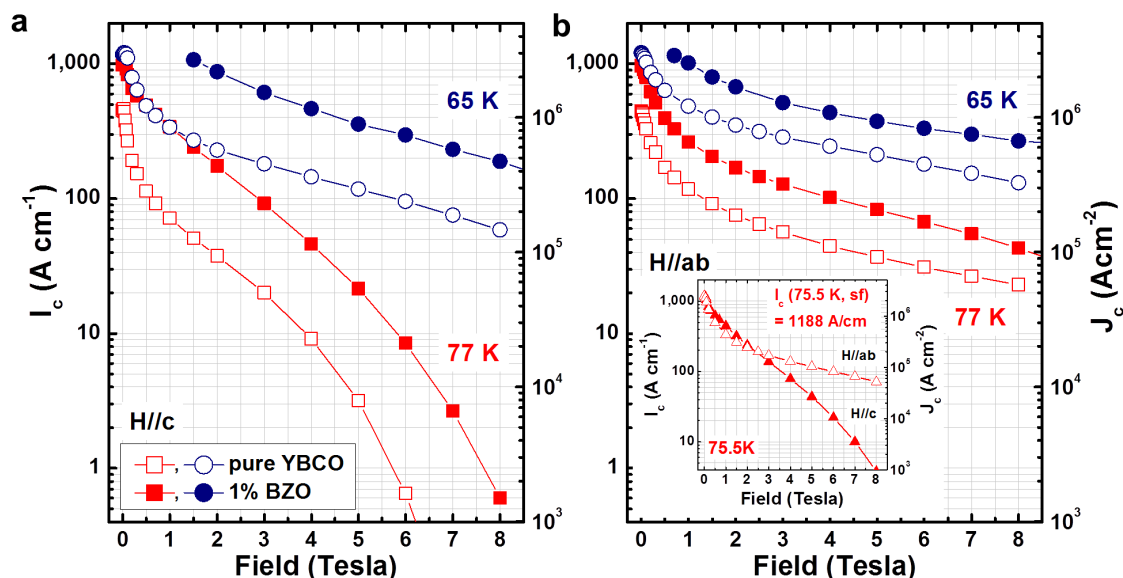
Figure 7 | The field dependent I_c at 77 K and 65 K for (a) $H//c$ and (b) $H//ab$ with the magnetic field up to 8 T for un-doped and 1 vol% BZO-doped, 4 μm thick YBCO films. The inset of Fig. 7(b) shows $I_c(H)$ data measured at 75.5 K for the BZO-doped thick film.

much BZO doping is approximately required to accommodate vortices generated in a specific field range[16]. For instance, 1 and 2 vol% BZO should be the optimum levels to maximize the pinning and J_c performance at low fields of ~0.8 T and modest fields of ~6 T respectively, but the doping level should increase to 4 vol% at much higher fields around 15 T. 10 vol% BZO-doped samples contain very dense BZO defects aligned both parallel and perpendicular to the YBCO c-axis that may effectively enhance the pinning for fields over 15 T (see Fig. 3). However, significant reduction in YBCO phase volume fraction (proportional to the amount of BZO volume fraction) as well as the degradation of cube texture (see Fig. 1d) and T_c (see Table 1) via excess BZO doping should result in negative impacts on the J_c particularly at high temperatures of 77 K and 65 K, over any gain caused by the enhanced pinning via the BZO defects as shown in Figs. 4 and 5. When comparing the field ranges for which the 1–4 vol% BZO-doped films exhibit the highest $J_c(H,T)$ in Fig. 4 with the B_ϕ values estimated from the respective BZO column densities, we

find that the B_ϕ values are close to or within these field ranges. The results demonstrate that optimal BZO nanocolumns density to achieve the highest J_c is different at different fields and temperatures, dictating that the number density of columnar defects is an effective way to achieve the highest J_c at any targeted field-temperature range.

Understanding of the effect of BZO doping on $J_c(H, \theta)$ at 77 K and 65 K for YBCO + BZO nanocomposite films provides key information to achieve high I_c performance at technically important field-temperature ranges for various electric power applications, such as i) 0–0.5 T, 65–77 K (for underground transmission cable, transformer, and fault current limiter) and ii) 3–5 T, 65 K (for large-scale motors and generators)[15]. Growth of a single layer YBCO film with high I_c (77 K, sf) over 1000 A cm^{-1} has been considered a very challenging work due to an exponential decay of critical current density, J_c, making a proportional increase in I_c with the film thickness not feasible. The decay in J_c with thickness can be attributed to a number of factors including roughening of film, loss of epitaxy or degradation of texture and reduction in the defect density of naturally formed defects[26,29,30]. To date, there have been only a few reports on fabrication of a single layer, thick YBCO films having self-field I_c close to or over 1000 A cm^{-1} at 75.5–77 K[27,28,31,32]. Very recently, I_c (77 K, sf) of 1018 A cm^{-1} was reported in 5.9 μm thick DyB$_2$Cu$_3$O$_{7-\delta}$ grown on the metallic templates prepared by inclined substrate deposition[32]. For the films grown on IBAD metallic templates, the self-field I_c of 944 A cm^{-1} at 77 K and 1007 A cm^{-1} at 76.55 K were obtained from a piece of the wire with 3.3 μm thick, 5 mol% Zr-doped (Y,Gd)BCO film[31]. For the films grown on single crystal substrates, the highest I_c of ~1500 A cm^{-1} at 75.5 K, self-field was reported from 9 μm thick YBCO films containing 5 mol% BZO and 5 mol% Y$_2$O$_3$[28]. Recent reports suggest that incorporation of BZO and (or) other defects into thick YBCO films is a very effective means to achieve the improved I_c at self-field as well as in magnetic fields[27,28,31].

Figure 9 compares the I_c and engineering critical current density, J_E, data at a field-temperature regime of 65 K, 3 T for the BZO-doped sample with those for the previous record performance HTS wires comprised of ~3 and 4 μm thick YBCO + BZO nanocomposite films[6,7]. The I_c(min) of 455 A cm^{-1} for the thick sample reported in this study corresponds to J_E of 43.7 kA cm^{-2} and 84.2 kA cm^{-2} with and without considering a 50 μm thick Cu stabilizer which may be needed in application. Both I_c and J_E performances are much higher than the previous values and are significantly exceeding the performance levels of 20 kA cm^{-2} needed for the applications[6].
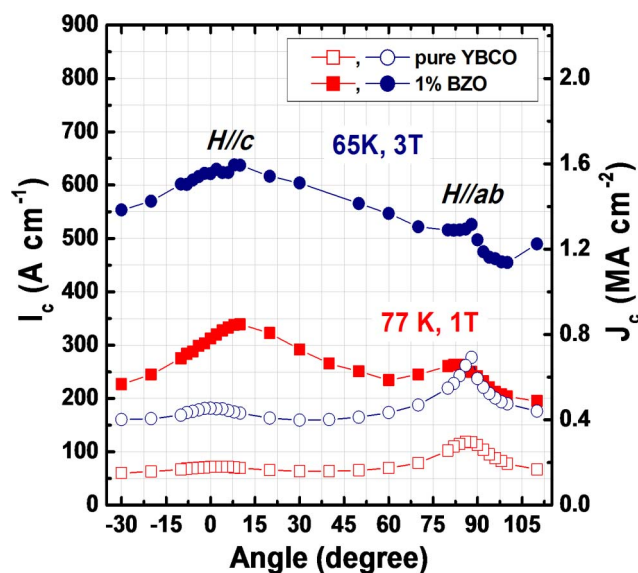

Figure 8 | Angular dependence of I_c for 4 μm thick, un-doped and 1 vol% BZO-doped, YBCO films measured at 77 K, 1 T and 65 K, 3 T.
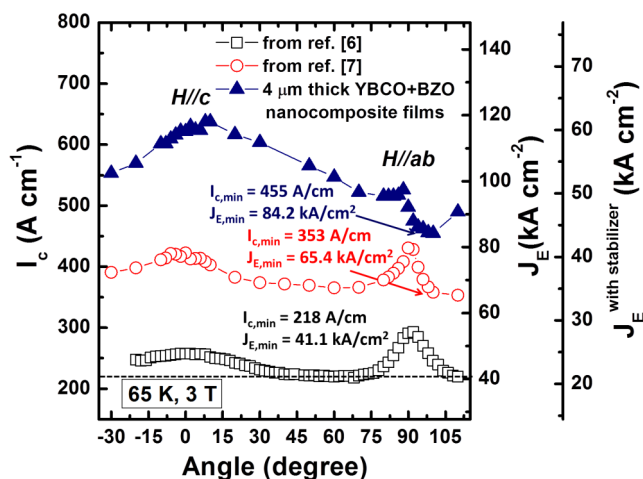
Figure 9 | Angular dependence of I_c and J_E for a 4 μm thick film of YBCO + 1 vol% BZO at a temperature-field regime of 65 K and 3 T. For comparison, I_c and J_E data for 3 and 4 μm thick YBCO + BZO films previously reported in refs. [6] and [7] are also plotted with open symbols. Since the total thickness of the 4 μm thick samples including substrate (~54 μm) considered for the J_E calculation is slightly different from that of the 3 μm thick sample (~53 μm) plotted together in the figure, J_E values for the 3 μm thick film sample are 2% or 1% (when considering additional 50 μm Cu stabilizer) higher than the J_E values plotted in the graph.

Higher I_c and J_E can provide wider gap from the operating current levels of a given application and thus, are always highly desirable as a greater safety buffer, to further reduce AC losses, and to avoid exceeding I_c locally due to any perturbation.

In summary, we systematically investigated the influence of BZO nanocolumnar defect density on structural and superconducting properties of YBCO + BZO nanocomposite films. The nanocomposite films with up to 4 vol% BZO contents have highly cube-textured, epitaxial YBCO phase and BZO nanophase with the morphology of vertically ordered nanocolumns. Compared to the un-doped sample, the 1–4 vol% BZO-doped samples showed a significantly improved J_c performance for entire magnetic field ranges with much higher F_P and smaller α values due to the presence of strong pinning via BZO columnar defects. More importantly, we show that the optimum density of BZO nanocolumnar defects is strongly field-dependent and thus, different BZO doping levels are needed to optimize pinning and to achieve the highest J_c properties at different magnetic fields, particularly when the field is parallel to the orientation of BZO defects, $H\|c$. Finally, we have fabricated thick, single-layer nanocomposite films with the controlled BZO concentration showing a self-field I_c of ~1000 A cm^{-1} at 77 K and the record I_c(min) of 455 A cm^{-1} at 65 K and 3 T ever reported from HTS films fabricated on metallic templates.

Methods

All YBCO films with and without different vol% of BZO were prepared by pulsed laser deposition (PLD) using a KrF (λ = 248 nm) excimer laser at a repetition rate of 10 Hz. Laser energy density and substrate to target distance were optimized to be 2 J cm^{-2} and 5 cm, respectively. The PLD target (2 inch diameter, 0.25 inch thick) was made by mixing commercially available YBCO powder and BaZrO$_3$ nanopowder using standard ball mixer, followed by densification at 950°C for 2 h. The film growth temperature, T_s, was 790°C and the oxygen partial pressure, P(O$_2$), was 230 mTorr. All depositions were performed on IBAD-MgO templates with a LaMnO$_3$ cap layer that were supplied from Superpower Inc.

After deposition, samples were *in-situ* annealed at T_s = 500°C and P(O$_2$) = 500 Torr, and *ex-situ* annealed at 500°C for 1 h in flowing O$_2$ gas after depositing sputtered Ag electrodes onto the films. The 0.5 cm wide × 2 cm long sample was patterned into a ~0.2 mm wide bridge by laser-scribing, due to the limits on the maximum measuring current in the characterization system. The standard four-point probe method with a voltage criterion of 1 μV cm^{-1} was used for the transport measurements. Phase and textures of the films were characterized by X-ray diffraction

method. Microstructures were characterized by transmission electron microscopy using a Hitachi HF-3300 TEM/STEM with a secondary detector and an energy-dispersive x-ray spectrometer at 300 kV and field emission scanning electron microscopy using Hitachi S4800 FEG-SEM. TEM foils were prepared by the focus ion beam (FIB) technique, followed by low voltage ion milling and plasma cleaning.

1. Zheng, H. *et al.* Multiferroic BaTiO$_3$-CoFe$_2$O$_4$ nanostructures. *Science* **303**, 661–663 (2004).
2. Jamet, M. *et al.* High-curie-temperature ferromagnetism in self-organized Ge$_{1-x}$Mn$_x$ nanocolumns. *Nat. Mater.* **5**, 653–659 (2006).
3. Mohaddes-Ardabili, L. *et al.* Self-assembled single-crystal ferromagnetic iron nanowires formed by decomposition. *Nat. Mater.* **3**, 533–538 (2004).
4. Harman, T. C. *et al.* Quantum dot superlattice thermoelectric materials and devices. *Science* **297**, 2229–2232 (2002).
5. Goyal, A. *et al.* Irradiation-free, columnar defects comprised of self-assembled nanodots and nanorods resulting in strongly enhanced flux-pinning in YBa$_2$Cu$_3$O$_{7-\delta}$ films. *Supercond. Sci. Technol.* **18**, 1533–1538 (2005).
6. Kang, S. *et al.* High-performance high-T_c superconducting wires. *Science* **311**, 1911–1914 (2006).
7. Wee, S. H., Goyal, A., Zuev, Y. L. & Cantoni C. High performance superconducting wires in high applied magnetic fields via nanoscale defect engineering. *Supercond. Sci. Technol.* **21**, 092001 (2008).
8. Mele, P. *et al.* Ultra-high flux pinning properties of BaMO$_3$-doped YBa$_2$Cu$_3$O$_{7-x}$ thin films (M = Zr, Sn). *Supercond. Sci. Technol.* **21**, 032002 (2008).
9. Wee, S. H. *et al.* Formation of self-Assembled, double-perovskite, Ba$_2$YNbO$_6$ nanocolumns and their contribution to flux-pinning and J_c in Nb-Doped YBa$_2$Cu$_3$O$_{7-\delta}$ Films. *Appl. Phys. Exp.* **3**, 023101 (2010).
10. Wee, S. H. *et al.* Enhanced flux pinning and critical current density via incorporation of self-assembled rare-earth barium tantalate nanocolumns within YBa$_2$Cu$_3$O$_{7-\delta}$ films. *Phys. Rev. B* **81**, 140503(R) (2010).
11. Feldmann, D. M. *et al.* Improved flux pinning in YBa$_2$Cu$_3$O$_7$ with nanorods of the double perovskite Ba$_2$YNbO$_6$. *Supercond. Sci. Technol.* **23**, 095004 (2010).
12. Ercolano, G., Harrington, S. A., Wang, H., Tsai, C. F. & MacManus-Driscoll, J. L. Enhanced flux pinning in YBa$_2$Cu$_3$O$_{7-\delta}$ thin films using Nb-based double perovskite additions. *Supercond. Sci. Technol.* **23**, 022003 (2010).
13. Macmanus-Driscoll. *et al.* Strongly enhanced current densities in superconducting coated conductors of YBa$_2$Cu$_3$O$_{7-x}$ + BaZrO$_3$. *Nat. Mater.* **3**, 439 (2004).
14. Wee, S. H. *et al.* Self-Assembly of Nanostructured, Complex, Mulit-Cation Films via Spontaneous Phase Separation and Strain-driven Ordering. *Adv. Funct. Mater.* **23**, 1912 (2013).
15. Larbalestier, D., Gurevich, A., Feldmann, D. M. & Polyanskii, A. High-T_c superconducting materials for electric power applications. *Nature* **414**, 368 (2001).
16. Civale, L. Vortex pinning and creep in high-temperature superconductors with columnar defects. *Supercond. Sci. Technol.* **10**, A11 (1997).
17. Peurla, M. *et al.* Optimization of the BaZrO$_3$ concentration in YBCO films prepared by pulsed laser deposition. *Supercond. Sci. Technol.* **19**, 767 (2006).
18. Kang, S. *et al.* Flux-pinning characteristics as a function of density of columnar defects comprised of self-assembled nanodots and nanorods in epitaxial YBa$_2$Cu$_3$O$_{7-\delta}$ films for coated conductor applications. *Physica C* **457**, 41 (2007).
19. Mele, P. *et al.* Systematic study of the BaSnO$_3$ insertion effect on the properties of YBa$_2$Cu$_3$O$_{7-x}$ films prepared by pulsed laser ablation. *Supercond. Sci. Technol.* **21**, 125017 (2008).
20. Huhtinen, H., Irjala, M., Paturi, P., Shakhov, M. A. & Laiho, R. Influence of BaZrO$_3$ dopant concentration on properties of YBa$_2$Cu$_3$O$_{6+x}$ films in magnetic fields up to 30 T. *J. Appl. Phys.* **107**, 053906 (2010).
21. Wee, S. H. *et al.* Heteroepitaxial film silicon solar cell grown on Ni-W foils. *Energy Environ. Sci.* **5**, 6052 (2012).
22. Yang, H. *et al.* Self-assembled multilayers and enhanced superconductivity in (YBa$_2$Cu$_3$O$_{7-\delta}$)$_{0.5}$:(BaZrO$_3$)$_{0.5}$ nanocomposite films. *J. Appl. Phys.* **106**, 093914 (2009).
23. Cantoni, C. *et al.* Strain-Driven Oxygen Deficiency in Self-Assembled, Nanostructured, Composite Oxide Films. *ACS Nano* **5**, 4783 (2011).
24. Culity, B. D. & Stock, S. R. Elements of X-ray diffraction (3rd edition). *Prentice Hall: Upper Saddle River, NJ*, Chapter 3 (2001).
25. Puig, T. *et al.* Vortex pinning in chemical solution nanostructured YBCO films. *Supercond. Sci. Technol.* **21**, 034008 (2008).
26. Foltyn, S. R. *et al.* Relationship between film thickness and the critical current of YBa$_2$Cu$_3$O$_{7-\delta}$-coated conductors. *App. Phys. Lett.* **75**, 3692 (1999).
27. Feldmann, D. M. *et al.* 1000 A cm^{-1} in a 2 μm thick YBa$_2$Cu$_3$O$_{7-x}$ film with BaZrO$_3$ and Y$_2$O$_3$ additions. *Supercond. Sci. Technol.* **23**, 115016 (2010).
28. Zhou, H. *et al.* Thickness dependence of critical current density in YBa$_2$Cu$_3$O$_{7-\delta}$ films with BaZrO$_3$ and Y$_2$O$_3$ addition. *Supercond. Sci. Technol.* **22**, 085013 (2009).
29. Kang, B. W. *et al.* Comparative Study of Thickness Dependence of Critical Current Density of Yba$_2$Cu$_3$O$_{7-\delta}$ on (100) SrTiO$_3$ and on Rolling-assisted Biaxially Textured Substrates. *J. Mater. Res.* **17**, 1750 (2002).
30. Foltyn, S. R. *et al.* Materials science challenges for high-temperature superconducting wire. *Nat. Mater.* **6**, 631 (2007).
31. Aytug, T. *et al.* ORNL-Superpower CRADA: Development of MOCVD-based, IBAD-2G Wires. Presented at 2008 Annual Peer Review for the U.S. Superconductivity Program for Electric Systems, Crystal city, VA, USA, July

29–31, 2008, available at: http://www.htspeerreview.com/2008/pdfs/presentations/wednesday/2G/5_2g_ornl_superpower.pdf (Accessed on March 06, 2009).

32. Durrschnabel, M., Aabdin, Z., Bauer, M., Prusseit, W. & Eibl, O. DyBa$_2$Cu$_3$O$_{7-x}$ superconducting coated conductors with critical currents exceeding 1000 A cm^{-1}. *Supercond. Sci. Technol.* **25**, 105007 (2012).

Acknowledgments

Author contributions

S.H.W. designed experiment, prepared the samples by PLD, characterized structural properties of the samples by XRD and SEM, and wrote the manuscript. Y.L.Z. measured superconducting properties of the samples. C.C. carried out the TEM characterization of the samples. A.G. supervised the research work and discussed the results. All authors reviewed the manuscript.

Additional information